

Data Efficient Prediction of excited-state properties using Quantum Neural Networks

Manuel Hagelüken,^{1,*} Marco F. Huber,^{1,2} and Marco Roth^{1,†}

¹Fraunhofer Institute for Manufacturing Engineering and Automation IPA, Nobelstraße 12, D-70569 Stuttgart, Germany

²Institute of Industrial Manufacturing and Management IFF,
University of Stuttgart, Allmandring 35, Stuttgart, D-70569, Germany

(Dated: December 13, 2024)

Understanding the properties of excited states of complex molecules is crucial for many chemical and physical processes. Calculating these properties is often significantly more resource-intensive than calculating their ground state counterparts. We present a quantum machine learning model that predicts excited-state properties from the molecular ground state for different geometric configurations. The model comprises a symmetry-invariant quantum neural network and a conventional neural network and is able to provide accurate predictions with only a few training data points. The proposed procedure is fully NISQ compatible. This is achieved by using a quantum circuit that requires a number of parameters linearly proportional to the number of molecular orbitals, along with a parameterized measurement observable, thereby reducing the number of necessary measurements. We benchmark the algorithm on three different molecules by evaluating its performance in predicting excited state transition energies and transition dipole moments. We show that, in many instances, the procedure is able to outperform various classical models that rely solely on classical features.

I. INTRODUCTION

Computing molecular properties, such as potential energy surfaces (PES) is a valuable yet often resource-intensive task, making it a highly active research area. A detailed understanding of molecular properties in different geometric configurations is beneficial for various applications in material science, pharmacology, and chemistry [1–3]. The ability to predict molecular behavior improves and optimizes processes, leading to more efficient research and applications, such as the discovery of new drugs [4] and the development of catalysts [5].

There are several methods to calculate properties of interest such as ground states and their energies for different molecule sizes with varying precision. For small molecules, full configuration interaction methods [6] can be used to determine the exact ground states and energies in a given basis. Additionally, complete active space self consistent field (CASSCF) [7] methods allow the definition of an active space to reduce the problem size and obtain approximate solutions for larger molecules. Despite this and further advances, classical algorithms still struggle with large systems with strongly correlated electrons, as the exact description of these systems scales exponentially with their size [8]. Therefore, quantum computing algorithms such as the variational quantum eigensolver (VQE) [9] and quantum phase estimation [10] have been studied in the pursuit of a better scaling which is enabled by the exponential size of the quantum Hilbert space. However, these algorithms have their own drawbacks, particularly in the current era of noisy intermediate-scale quantum computing [11]. Notable problems include a high circuit depth, a large number of measurements [9],

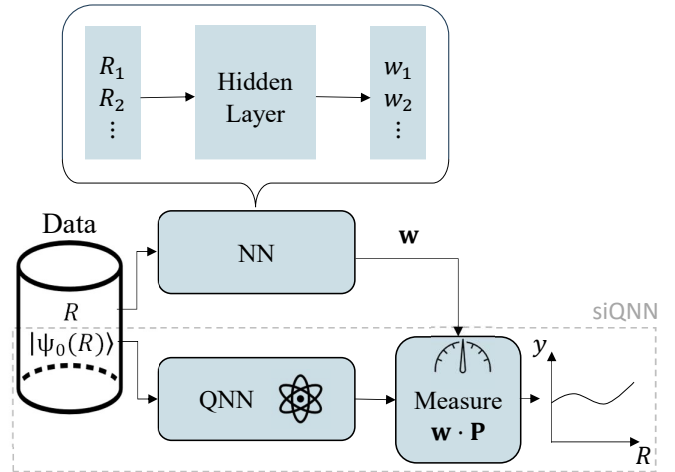


FIG. 1. Schematic overview of the model used in this study. The feature set, i.e., the input to the model is given by $\mathcal{X} = (|\psi_0(R)\rangle, R)$, where $|\psi_0(R)\rangle$ denotes the molecular ground state and R is the potentially multi-dimensional distance between the atoms. The model is trained to predict various target values y such as the transition energy ΔE to an excited state. The observable is a weighted sum of Pauli-strings \mathbf{P} , where the weights \mathbf{w} are learned by a classical NN [cf. Equation (3)]. Training this model involves a pre-training of the siQNN (dashed box) followed by an end-to-end training of the whole architecture.

and the necessity for a large overlap of the ansatz with the final state [12]. Consequently, recent studies have focused on combinations of classical and quantum algorithms, aiming to leverage the strengths of both approaches [13, 14].

Most methods, especially for quantum computing, are tailored to obtain ground states and their energies. However, for many chemical and physical processes, such as photochemical reactions, energy transfer, and the absorp-

* manuel.hagelueken@ipa.fraunhofer.de

† marco.roth@ipa.fraunhofer.de

tion and emission of light, excited states are of significant interest. An accurate calculation of these states and their energies is much more challenging because they are usually composed of more electronic configurations than the ground state [15]. Additionally, electron correlations are more pronounced, and they can have different spin multiplicities and symmetries. Furthermore, it is challenging to correctly differentiate between individual states due to effects such as (avoided) crossings [16]. There are several extensions to the commonly used quantum computing algorithms to calculate excited states, such as variational quantum deflation [17] or subspace-search VQE [18], but since these often are based on VQE they usually suffer from the same drawbacks.

To address these challenges we propose a quantum machine learning (QML) model that directly operates on the quantum mechanical ground state on a quantum computer (QC). The quantum state is measured using only commuting operators drastically reducing the overhead on the QC. The model includes a quantum neural network (QNN) and a classical neural network (NN) designed to efficiently calculate excited-state properties¹ for different geometric configurations of a given molecule. The architecture of the QNN is constructed to explicitly account for the symmetries of the ground state. The proposed model is able to predict these properties with only a few training data points which avoids costly excited state simulations. The overall procedure is sketched in Figure 1.

To assess the performance of our method, we compare it to well-known classical methods. We benchmark these models on three different molecules for various excited states. We calculate the transition energy of the ground state to excited states (ΔE) and the L_2 -norm of the transition dipole moments (TDM) between the ground state and excited states for varying interatomic distances. We find that using the ground state as an additional feature significantly improves the prediction quality, especially in the low-data regime.

In a related work [19] the first transition energies and TDMs are predicted by performing measurements with different observables on the ground state after a non-parametrized entangling layer. The measurement values are used as input for an NN that outputs the target functions. In [20] a deep neural network determines the parameters of a QNN that prepares excited states using variational quantum deflation or the subspace search VQE. While these approaches share a similar rationale regarding the benefits of interpolation in this context, our model predicts excited-state properties with a significantly lower number of training data points, by directly learning on the molecular ground state.

The remainder of this work is organized as follows. In Section II, we motivate and discuss the construction of the model and its training procedure. In Section III, we demonstrate the efficacy of the model in predicting excited-state properties from ground states of LiH, H₂, and rectangular H₄, and provide evidence for its data efficiency compared to several other models. Finally, in Section IV, we discuss our findings, the limitations of our model and study design, and propose directions for further research.

II. METHODS

In this section, we define the problem and present the QML model. We describe how the ground state of a molecule can be obtained on a QC utilizing the Jordan-Wigner transformation. From this, we discuss relevant symmetry considerations and use this insight to tailor our model to the task of predicting excited-state properties from the ground state.

A. Molecular States on a QC

The Fermionic Hamiltonian of a molecule in second quantization is of the form

$$H = \sum_{pq} h_{pq} a_p^\dagger a_q + \frac{1}{2} \sum_{pqrs} h_{pqrs} a_p^\dagger a_q^\dagger a_r a_s, \quad (1)$$

where h_{pq} and h_{pqrs} are the Coulomb overlap and exchange integrals, and a_i^\dagger and a_i are Fermionic creation and annihilation operators. To make this Hamiltonian computationally tractable, we restrict the orbitals to an active space containing only the most important contributions to our quantity of interest. To analyze molecules on a QC, the Fermionic operators need to be mapped to qubit operators. In this work, we use the Jordan-Wigner mapping due to its straightforward physical interpretation [21]. Using this mapping, the creation operators can be expressed as

$$a_p^\dagger = \frac{1}{2} (X_p - iY_p) \prod_{j=1}^{p-1} Z_j,$$

where X , Y , and Z are the Pauli operators of the i -th qubit. The annihilation operator is given analogously. From this we obtain a qubit Hamiltonian

$$H_{\text{qubit}} = \sum_{i=0}^K c_i P_i, \quad (2)$$

where the coefficients c_i are determined by h_{pq} and h_{pqrs} and P_i are Pauli-strings determined by the mapping.

With this mapping, each spin-orbital is represented by a qubit, where an excited qubit state corresponds to an

¹ We use ‘‘excited-state property’’ not only for intrinsic properties of the excited state but also to excited state related properties such as transition energies.

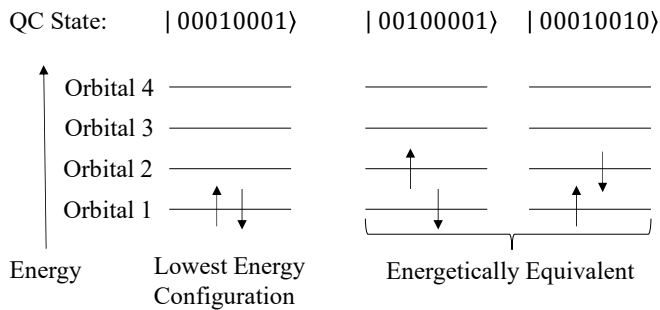


FIG. 2. A simple illustration of the symmetry of several electronic ground state configurations for H_2 with four considered orbitals prepared on the QC using the Jordan-Wigner mapping.

occupied orbital. Since electrons can be either spin-up (α -electron) or spin-down (β -electron), $2n_{\text{orb}}$ qubits are needed to represent a molecule with n_{orb} orbitals. The exact ordering of qubits to spin-orbitals can vary. In this work the first n_{orb} qubits represent one type (e.g., α) of electrons, and the second n_{orb} qubits represent the other type of electrons. Furthermore, the first qubit of both spin-subsets, i.e., qubit 0 and qubit n_{orb} , correspond to the first orbital (lowest energy configuration), the second to the second orbital, and so on. This ordering of orbitals by energy is established near the equilibrium configuration and is preserved throughout the dissociation curve to enhance the generalization performance of the QNN across the dissociation.

We consider molecules in an isolated environment, resulting in a spin-degeneracy between the α and β orbitals. Figure 2 illustrates three spin configurations and their corresponding Jordan-Wigner mapped states for the example of H_2 . Near the equilibrium the lowest energy configuration has the highest amplitude in the ground state. However, higher energy configurations also contribute to the ground state but with smaller amplitudes. Each configuration is associated with a computational basis state on the QC. The squares of the amplitudes of these computational basis states represent the probabilities of electrons occupying the corresponding spin-orbitals. As the molecule dissociates, the shapes of the orbitals change, leading to variations in the occupation probabilities of the spin orbitals. Consequently, the amplitudes of the computational basis states in the ground state change accordingly. In the following section, we design a QNN to read and process these amplitudes and their variations to derive the target value y (in our case an excited-state property in a given geometric configuration) using training data points. For the theoretical justification for why it is possible to predict properties of excited states from the ground state, we refer to [19].

B. Model Ansatz

An intuitive approach to derive excited-state properties from the ground state would be to use the QNN as a parametrized excitation operator and measure the resulting state with the observable corresponding to the desired property. However, there are two problems with this approach, which we address with specific design choices of our model.

First, the observable $O = \mathbf{wP}$ [e.g., Eq. (2)] is generally a linear combination of many non-commuting Pauli-strings P with coefficients \mathbf{w} . This leads to a significant overhead on the QC, as only commuting operators can be measured on the same quantum state. We address this issue by defining an observable that consists solely of commuting Pauli-strings, specifically strings that only contain Pauli-Z operators. This observable has the form

$$O(\mathbf{w}) = w_1 \mathbb{1} + w_2 (Z_0 + Z_{n_{\text{orb}}}) + w_3 Z_0 Z_{n_{\text{orb}}} + \dots, \quad (3)$$

where $\mathbb{1}$ is the identity operator. The observable is constructed such that the result remains unchanged when the first n_{orb} qubits are exchanged with the last n_{orb} qubits, as discussed in Section II A. In this work, the qubits corresponding to the first orbital contribute equally to the final sum. Additional measurements on the qubits corresponding to higher orbitals can be incorporated following this approach. Measuring $O(\mathbf{w})$ requires that the QNN learns a basis change where this simplified observable measures the corresponding target function. This approach drastically reduces the measurement-related overhead on the QC.

The second challenge is that both the excitation operator and the observable generally depend on the geometric configuration of the given molecule. In this work, R is a scalar describing the distance between the atoms of the molecule, but in general R can be a multidimensional vector. Although one might hope that the R dependency could be negligible or that the QNN could project into an R -independent space, we explicitly consider these R dependencies by introducing a small classical NN. This NN takes R as input and outputs the weights w_i in Equation (3). The linear combination of these operators constitutes the output of the model. Therefore, the NN is designed to learn and account for the R dependence of the excitation operator and the observable in the model. An example of the overall structure of the model is depicted in Figure 1.

For the QNN, we choose a structure that is designed to be efficiently trainable and to have a useful bias towards the overall operations it is meant to perform. To integrate the molecular symmetry into the QNN, we make the QNN invariant under the exchange of α and β -electrons. This can be achieved by letting all operators and observables, along with their parameters acting on the first n_{orb} qubits, also act on the last n_{orb} qubits.

To enhance the trainability, the structure of the QNN is partly inspired by quantum convolutional neural networks, which are known to avoid barren plateaus and

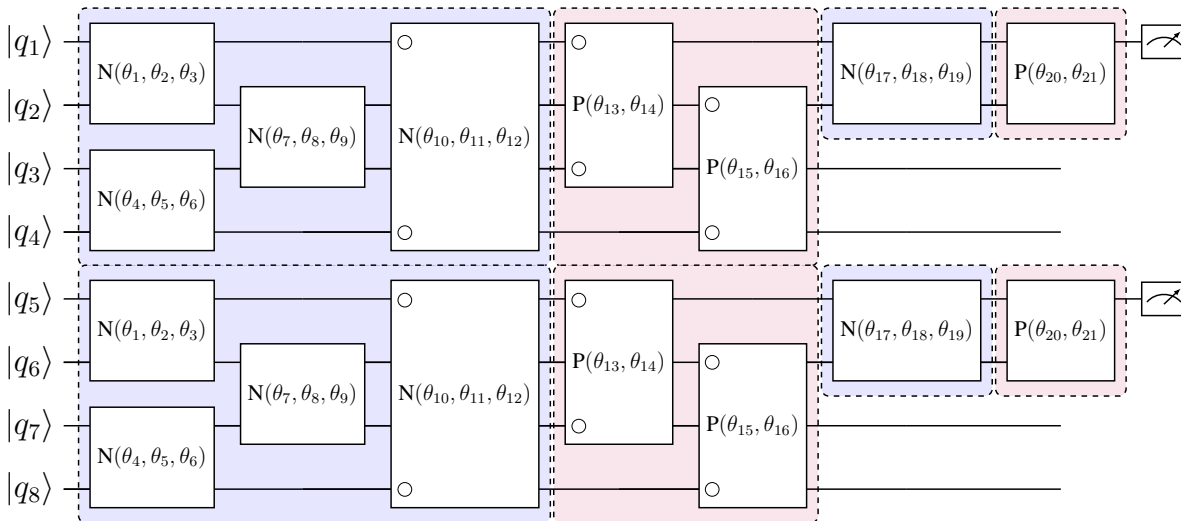


FIG. 3. An example of the structure of the QNN ansatz for H_2 with 4 orbitals and 2 electrons. Here, θ_1 – θ_{21} are trainable parameters and q_1 – q_8 denote the qubits. The two-qubit gate $N(\theta_i, \theta_j, \theta_k) = \exp[i(\theta_i XX + \theta_j YY + \theta_k ZZ)]$ can realize every two qubit unitary [22] and $P(\theta_n, \theta_m)$ is a two qubit entangling gate that acts as a pooling operation [23]. When gates act on non-neighboring qubits, circles in the gates mark the qubits on which the gates are applied.

have a number of parameters that scale logarithmically [23]. Together with the given symmetry restriction the number of parameters is further reduced, scaling linearly with the number of orbitals considered. Specifically, when pooling to two qubits the number of parameters is $n_{\text{params}} = 8(n_{\text{orb}} - 1) - 3$. The relevance of the findings in paper [24] regarding the simulatability of quantum convolutional neural networks is discussed in Chapter IV. The QNN consists of alternating two-qubit operation layers. The first layer (N) is designed for maximal expressivity, while the second layer (P) is a pooling layer designed to entangle the given qubits. After each pooling layer, the qubit with the larger index in the pooling operation is discarded. Qubits associated with orbitals of larger indices, as defined in Section II A, are discarded earlier because the occupation probability in the near-equilibrium ground state generally decreases with increasing orbital indices. These operations are repeated until only two qubits remain, due to the small size of the molecules considered. However, for larger systems, one could repeat this process until the number of remaining qubits equals the number of electrons in the system. Our aim for the QNN is to transform the ground state into a state that, when measured, returns an approximation of the desired target state observable. Figure 3 shows an example of such a QNN for H_2 with 4 orbitals. We call the resulting symmetry-invariant QNN combined with an NN “siQNN-NN”. Note that we have chosen the particular QNN architecture in Figure 3 for its computational efficiency. However, the proposed method of letting a QNN operate directly on ground states is not restricted to this specific choice.

C. Training

We train the siQNN-NN model in two steps. In the first step, only the symmetry-invariant QNN (siQNN) is trained (gray dashed outline in Figure 1). In this step, the weights w_i [cf. Equation (3)] are not parameterized by an NN but rather learned directly through gradient descent. The aim of this pre-training is to navigate the parameters of the siQNN towards a favorable region in the reduced optimization landscape, i.e., the landscape of the siQNN without the NN. This is followed by an end-to-end training of the siQNN-NN model. Here, the QNN is initialized with the pre-trained parameters while the NN parameters are initialized randomly.

In the best case, the siQNN parameters are already optimal after pre-training, and the model output is similar to the target function. Then, the NN only fine-tunes the siQNN output towards the target function in regions where it is necessary to account for minor effects of the R dependence. However, in some cases (e.g., the target function $\|\mu_{0,S_2}\|_2$ for LiH, see Figure 4) the siQNN is not able to adequately describe the target function on its own, due to its restricted expressiveness. Then, the pre-training might converge to parameters that are sub-optimal for the complete siQNN-NN model. In this case, the combined training becomes more important and the NN is used to account for the pronounced R -dependence.

In both training steps, we use an Adam [25] optimizer with the mean squared error (MSE) as a loss function. Training is terminated if one of three criteria is met: 1) if the training loss decreases below a predefined target loss \mathcal{L}_t , 2) if the training loss does not improve over a

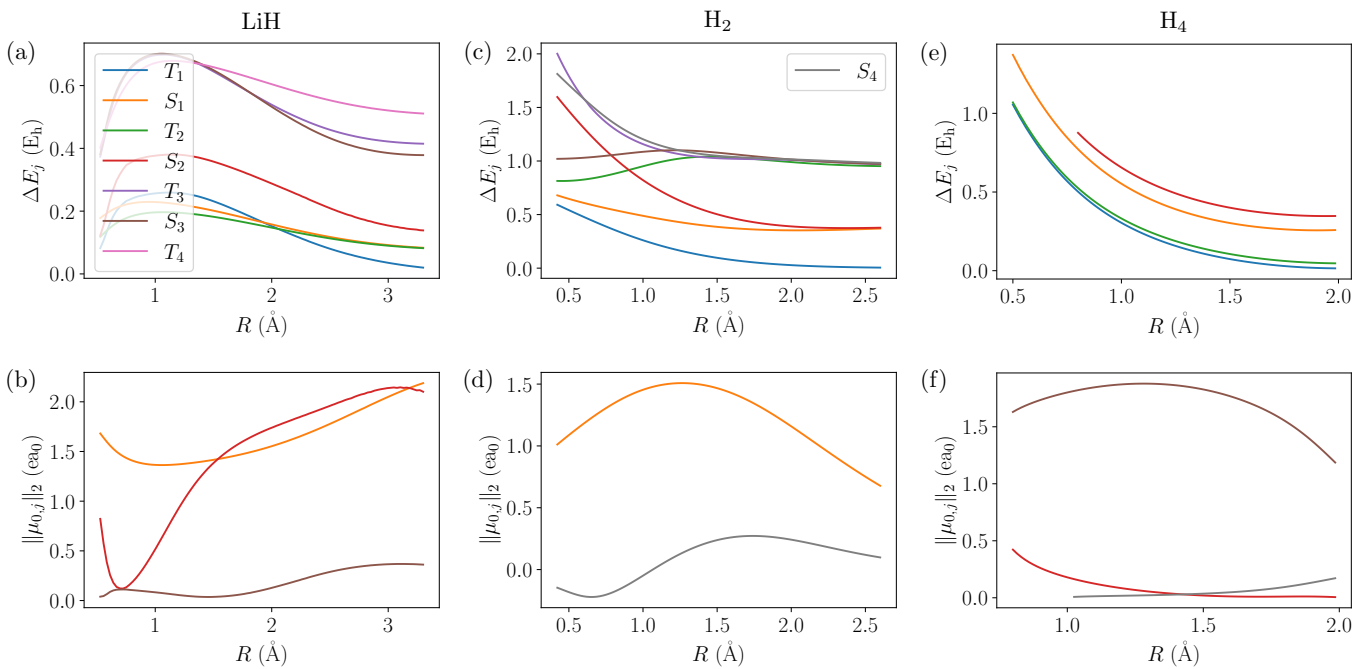


FIG. 4. The target functions for LiH in (a) and (b), for H₂ in (c) and (d), and for H₄ in (e) and (f) in the 6-31G basis. In (a), (c), and (e) the transition energies ΔE_j for the four energetically lowest excited singlet and triplet states, that do not exhibit avoided crossings, are shown in Hartree E_h. In (b), (d), and (f) the non-zero TDMs of those states are shown in units of elementary charge e and the Bohr radius a_0 . All values are obtained via exact diagonalization of Equation (2).

certain number of iterations, or 3) if a maximum number of iterations is reached.

III. RESULTS

In this section, we evaluate the performance of the model on three exemplary molecules (LiH, H₂, and H₄). We perform regression on a variety of transition energies and dipole moments and compare the result to other classical ML models.

A. Datasets

In selecting appropriate example molecules to benchmark the model, we try to satisfy a trade-off between sufficient complexity and reasonable computational costs. We therefore choose LiH which, with $n_{\text{orb}} = 5$, is small enough to be simulated, trained, and extensively studied while already exhibiting interesting electronic characteristics. Additionally, to analyze the scalability of our model we also benchmark it on H₂ with $n_{\text{orb}} = 4$ and rectangular H₄ with $n_{\text{orb}} = 6$.

For each molecule, we calculate the corresponding Hamiltonian Equation (1) in an active space of n_{orb} orbitals using CASSCF with the “6-31G” basis set using PySCF [26]. We then obtain the respective qubit Hamiltonian Equation (2) using Qiskit [27]. The qubit Hamiltonian is diagonalized to derive the eigenstates $|\psi_j\rangle$ and

their energies E_j . From these we construct a regression dataset $\mathcal{D} = (\mathcal{X}, \mathcal{Y})$ for each molecule with $y \in \mathcal{Y} \subset \mathbb{R}$. The features consist of the ground states $|\psi_0(R_k)\rangle$ and the corresponding atomic distance R_k , i.e., $\mathcal{X} = (\mathcal{S}, \mathcal{R})$, where $\mathcal{S} = \{|\psi_0(R_0)\rangle, \dots, |\psi_0(R_M)\rangle\} \subset \mathbb{C}^{2^{2n_{\text{orb}}}}$ and $\mathcal{R} = \{R_0, \dots, R_M\} \subset \mathbb{R}$ with the number of data points M . In our experiments, we fix $M = 100$ if not mentioned otherwise and select data points with equal spacing in R .

In our benchmarks, we consider two different excited-state properties for the targets y : transition energies and TDMs. The transition energies are given by $\Delta E_j = E_j - E_{S_0}$, where $j \in \{S_1, S_0, \dots, T_1, T_2, \dots\}$ labels the corresponding excited singlet (S_i) and triplet states (T_i). TDMs are given by

$$\|\mu_{0,j}(R)\|_2 = \|\langle \psi_0(R) | \boldsymbol{\mu} | \psi_j(R) \rangle\|_2.$$

Here, $\|\cdot\|_2$ is the L_2 norm, $|\psi_j(R)\rangle$ with $j \in \mathcal{S}$ is the j -th excited state, and $\boldsymbol{\mu}$ is the dipole moment operator. In calculating the TDMs, we account for possible sign changes to ensure differentiability across the chosen R spectrum.

For each molecule, we calculate the first four excited singlet and triplet state energies and the corresponding non-zero TDMs, see Figure 4. The upper row displays the transition energies, while the lower row shows the TDMs. The functions exhibit different degrees of complexity. Thus, it can be expected that different numbers of data points are required to describe each function with similar accuracy. The TDMs for LiH are comparatively complex, whereas the transition energies for H₄

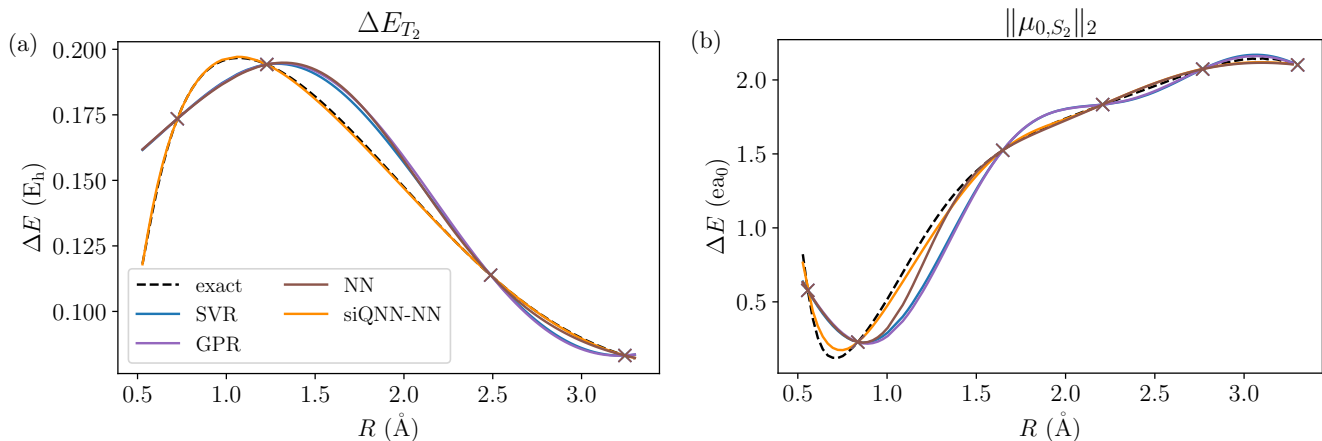


FIG. 5. The predictions (solid lines) of (a) ΔE_{T_2} and (b) $\|\mu_{0,S_2}\|_2$ for LiH for various models trained on specific trainings datasets. In (a) four training data points (marked by crosses) and in (b) six training data points are used. The exact target functions are represented by dashed lines. In (a) the best MSE score on the test dataset is achieved by the siQNN-NN, with a value of $2.6 \times 10^{-7} E_h^2$. The second best test MSE score is obtained by the SVR, with a value of $9.1 \times 10^{-5} E_h^2$. In (b) the best MSE score on the test dataset is achieved by the siQNN-NN, with a value of $8.3 \times 10^{-4} E_h^2$. The second best test MSE score is obtained by the NN, with a value of $3.7 \times 10^{-3} E_h^2$.

and partially for H_2 are relatively simple. Furthermore, several target functions for a given molecule mostly differ by a constant offset, and therefore the performance of the models on these functions are similar. To avoid learning problems, we only retain the states in which the entire R region, from repulsion to dissociation, does not exhibit obvious avoided crossings [13]. During training, we scale R and all target values to the interval $[-1, 1]$.

In the following experiments, we assume that the molecular states on the QC are provided by some quantum algorithm. In the NISQ era, this could for example be done using VQE. To isolate the performance of the model from potential impurities in the input quantum states, we initialize the quantum register directly to state vectors obtained by diagonalizing the qubit Hamiltonian Equation (2).

We compare the performance of the siQNN-NN model to well-known classical models with a reduced feature space, i.e., $\bar{\mathcal{X}} = \mathcal{R}$. The models are trained only on this reduced feature space because the size of the state vector of a molecular ground state is $2^{2n_{\text{orb}}}$. Even if the amplitudes were available classically (e.g., by state tomography), including the molecular states in \mathcal{X} would make the feature dimension more than an order of magnitude larger than the size of the training dataset used in this study, which prevents a generalization for these models. However, in Section IV we argue, that it might be possible to construct a purely classical model, that manages to extract valuable information from the large state vector of the molecular states, but this would require a much more sophisticated ansatz and would therefore be an interesting follow-up research topic.

B. Model Details

For the siQNN-NN, we use an NN with a single hidden layer comprising 41 parameters with a “tanh” activation function for the hidden layer. The NN is implemented using PyTorch [28], while the QNN is implemented in sQULearn [29] and Qiskit, and then integrated into the model and trained using PennyLane [30] with state vector simulations. Pre-training is performed with a large learning rate of 0.5 and a maximum of 1,000 iterations to broadly explore the optimization landscape and prevent getting stuck in local minima. The subsequent training of the siQNN-NN is conducted with a learning rate between 0.005 and 0.05 and a maximum of 2,000 iterations to enable smooth convergence. The performance of the model learning on the ground state derived after pre-training labeled siQNN is also compared to the performance of the classical models in the following.

We compare the performance of these models to a purely classical NN that has the same structure as the siQNN-NN, but without the quantum component. The model is trained on the reduced feature space $\bar{\mathcal{X}}$. To ensure comparability, the number of parameters in the NN is equal to the total number of parameters in the siQNN-NN (the sum of parameters in the QNN and the NN). This model is trained until convergence or until the target training loss \mathcal{L}_t is reached. Additionally, a support vector regressor (SVR) and a Gaussian process regressor (GPR) with a radial basis function kernel are implemented using scikit-learn [31]. Their hyperparameters are optimized using a grid search, where the performance of the hyperparameters is evaluated on the training dataset.

Since we operate on data that is very computationally expensive, especially for large molecules, we are interested in a low-data regime. In this regime, a sepa-

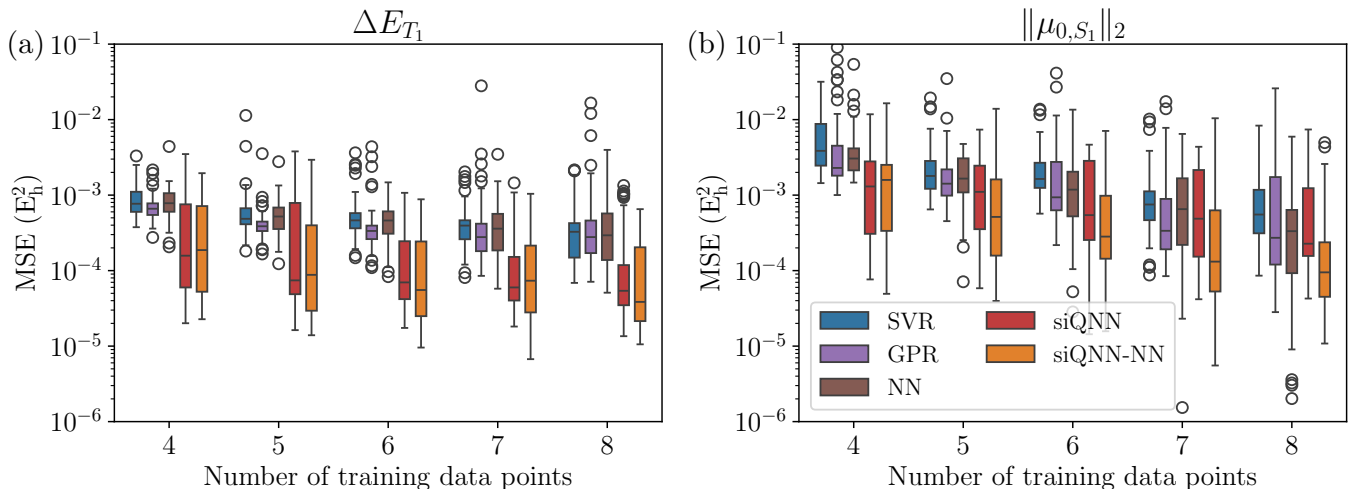


FIG. 6. Box plots of the MSE on the test datasets for 50 randomly sampled datasets \mathcal{D}_t^L for the given models and training dataset sizes L for LiH. (a) shows results for predicting the first transition energy ΔE_{T_1} and (b) the same for the norm of the first non-zero TDM μ_{0,S_1} .

rate validation dataset is can not meaningfully be defined because having a validation set with only a couple of data points would cause significant information leakage from the validation set. Furthermore, separate validation dataset is not required, as there is no need for hyperparameter optimization due to the low influence of the hyperparameters on the accuracy. Nevertheless, a validation dataset, the training of the (Q)NN-based model cannot be stopped when performance on the validation dataset worsens and overfitting occurs, but instead is stopped when $\mathcal{L}_t = 1 \times 10^{-6} E_h^2$ is reached on the training dataset. We choose this particular value as it is just below chemical accuracy. Recent work has found that QML methods generally avoid systematic overfitting of the training data, making the low data regime potentially interesting for QML methods in general [32].

C. Benchmark

To draw conclusions about the performance of the models based on training dataset size independent of the specific choice of points, we sample multiple training datasets $\mathcal{D}_t^L \subset \mathcal{D}$. Each set \mathcal{D}_t^L contains L data points. For each L , we sample 50 independent datasets, i.e., $l = 1, \dots, 50$. As a test set, we choose the remaining data points for each l and L , i.e., $\mathcal{D} \setminus \mathcal{D}_t^L$. In the following, all MSE scores shown are derived from the test dataset. We aim to simulate a realistic scenario where sampling is expensive, and the approximate locations of three different regions (attractive, equilibrium, and repulsive) along the dissociation curve are known. From each of these regions one data point is randomly chosen to account for the different behaviors in these regions. These three data points are then used as initial points for a Bayesian optimization, which determines the final

data points in the training dataset \mathcal{D}_t^L . However, using a less informed sampling method, e.g., equally spaced training data points from random subsets of the given dataset yields similar results.

1. LiH

For LiH we train the models on seven transition energies and three TDMs, see Figure 4 (a) and (b). We consider interatomic distances R between 0.5–3.3 Å.

Figure 5 shows two examples where the inference of the siQNN-NN along with three classical models is shown. The models have been trained on datasets of size (a) $L = 4$ with the transition energy ΔE_{T_2} and (b) $L = 6$ with the TDM $\|\mu_{0,S_2}\|_2$. In (a) one can observe that all models besides the siQNN-NN agree on predicting a similar and more intuitive shape, given the training data points. The siQNN-NN has a less intuitive fitting bias, that matches the target function significantly better with an MSE score more than two orders of magnitude smaller than that of the other models. In (b), one can observe a similar behavior of the models, except that the kernel methods (SVR, GPR) exhibit overfitting. Here, the siQNN-NN fit has an MSE more than four times lower than the next best classical model. These observations are consistent with the results of the subsequent systematic study.

Figure 6 (a) exemplarily shows a boxplot of the MSE for various models for the first transition energy ΔE_{T_1} . The median MSE on the test set for the quantum models (siQNN and siQNN-NN) are similar to each other and nearly an order of magnitude lower than those of the classical models (SVR, GPR, NN), which themselves perform similarly across all training dataset sizes considered. Additionally, the variation of the MSE for the siQNN and siQNN-NN is significantly larger than that of

the classical models. This is because, for some training dataset samples, the training points poorly represent the overall shape of the target function, causing all models to perform equally poorly. For other training data point combinations, the siQNN and siQNN-NN outperform the classical models by about an order of magnitude in MSE. In cases where other transition energies than ΔE_{T_1} are chosen, the performance of the models is similar (shown in Appendix A).

Figure 6 (b) shows the MSE for the first TDM $\|\mu_{0,S_1}\|_2$. Here, the overall discrepancy between quantum and classical models is smaller than for ΔE_{T_1} . Nevertheless, for larger training dataset sizes, the siQNN-NN still performs about half an order of magnitude better than the classical models, but the performance of the siQNN is similar to that of the classical models. For the other TDMs (shown in Appendix A), the siQNN and siQNN-NN perform similarly or worse than the classical models for small training dataset sizes; however, as the training dataset size increases, the siQNN-NN significantly outperforms the other models. This indicates that the siQNN alone is not expressive enough to account for the R dependence. This can be alleviated by parametrizing the interatomic distance with a classical NN.

To summarize the performance across the different target functions for LiH, Figure 7 (a) shows the average rank of the models by MSE on these ten target functions for different training dataset sizes, with the smallest MSE ranked first. The best possible rank is 1.0, indicating that the model is the best for all target functions and training dataset samples, while a ranking of 5.0 represents the worst possible outcome. One can observe, that for the case $L = 4$, the siQNN performs best, followed by the siQNN-NN. For all other training dataset sizes, the siQNN-NN is the best-performing model, achieving peak performance at a training dataset size of $L = 8$, with a mean ranking of 1.646 ± 0.045 , where the second-place ranking is nearly double that value. The ranking of the siQNN declines with increasing training dataset size. This can be explained because the MSE score for the siQNN remains roughly constant while the performance of the other models improves with increasing training dataset size. This indicates that, in most cases, the siQNN finds a good approximation of the target function but is not expressive enough to find a set of parameters that fits the targets for all values of R . Among the classical models, the GPR performs the best, while the NN and SVR perform similarly.

2. H₂

For H₂ we train the models on seven transition energies and two TDMs, see Figure 4 (c) and (d). We consider interatomic distances R between 0.4–2.6 Å. Figure 7 (b) shows the ranking plot for the performance on H₂. As for LiH, one of the ground-state based models (siQNN or siQNN-NN) is predominantly the best-performing model,

with the only exception occurring at eight training data points, where the GPR outperforms the siQNN-NN, and the NN performs within the error range of the siQNN-NN. This is likely due to the fact that several target functions for H₂ are relatively trivial. Furthermore, the performance of the NN in the case of H₂, with an average rank of about 2.5, is significantly better than in the case of LiH. This indicates that lower complexity of the molecule is more compatible with the small NN.

Some of the target functions (Figure 4), such as ΔE_{T_1} , are relatively trivial, which is also reflected in the MSE scores of the models (shown in Appendix A). For these trivial target functions, the MSE for some classical models is already in the order of 10^{-5} with a training dataset size of four, and it decreases with increasing training dataset size down to about 10^{-7} . The quantum-enhanced models perform about an order of magnitude worse than the classical models for these functions because the increased feature space adds additional complexity to the learning task, which introduces unnecessary complexity and therefore overfitting. Further, as explained in Section II C, we stop training the (Q)NN-based models when $\mathcal{L}_t = 10^{-6}$ is reached. Therefore, if the test MSE of these models is close to or below 10^{-6} , further training with a smaller \mathcal{L}_t could reduce the test MSE even further for these models, potentially aligning them with models that do not use a \mathcal{L}_t such as the kernel methods, i.e., SVR or GPR. Consequently, for target functions and training dataset sizes with MSE values close to or below \mathcal{L}_t , comparisons between the (Q)NNs and the kernel methods are limited significance. This effect becomes more relevant for increasing training dataset size.

For more complex target functions, such as ΔE_{T_2} , where the test MSE score of the classical models is mostly above 10^{-5} for several training dataset sizes, the siQNN-NN outperforms the NN model and the other classical models for small L . For some target functions, kernel methods exhibit MSE scores that are orders of magnitude larger than the MSE score of the NN. This is mostly due to overfitting which is difficult to prevent in the low-data regime.

Overall, the classical models outperform the quantum-enhanced models for relatively trivial target functions. However, for more complex target functions, the quantum-enhanced models outperform the classical models, as the additional information from the ground state can be leveraged to achieve better prediction performances.

3. H₄

The target functions for H₄ are shown in Figure 4 (e) and (f). Three transition energies are presented over the region 0.5–2.0 Å for R and the distance between the Hydrogen atoms on the other axis of the rectangular H₄ is equal to 2.0 Å for all target functions. Additionally, three TDMs are shown in reduced regions beyond an

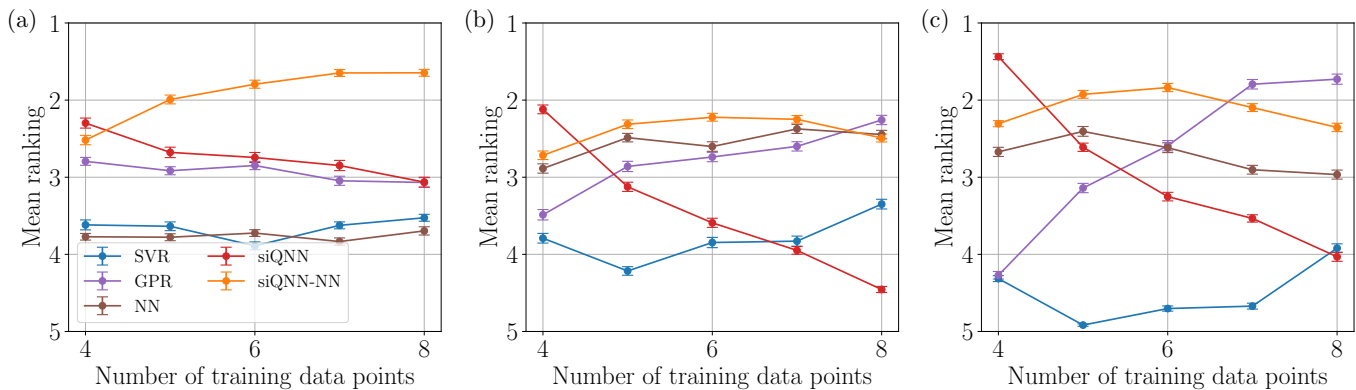


FIG. 7. Average rank of the models, broken down by training dataset size for (a) LiH, (b) H₂, (c) and rectangular H₄. Each point represents the relative rank of the respective model compared to all other models averaged over all considered targets and training samples for a molecule. The error bars indicate the standard errors of the mean values of those mean rankings.

avoided crossing (0.8–2.0 Å and 1.0–2.0 Å). Furthermore, one transition energy is considered in the reduced region beyond the avoided crossing (1.0 and 2.0 Å) to at least include the first two singlet and triplet energy states. The corresponding dataset sizes are reduced to the data points within the reduced regions, i.e., $M = 80$ and $M = 65$, respectively.

The ranking plot for H₄ is shown in Figure 7 (c). It is similar to the one for H₂, but the SVR performs worse overall, while the GPR performs better, already being the best model for seven training data points. The siQNN-NN performs significantly better than the NN for all training dataset sizes with a peak performance of 1.837 ± 0.053 for six training data points, while the siQNN has a peak performance of 1.437 ± 0.038 for four training data points.

IV. DISCUSSION

In this work, we investigated the effectiveness of enhancing the performance of a machine learning model trained to predict excited-state properties of a molecule in different geometric configurations. We achieved this by training a QNN directly on the molecular ground state to extract information from the wave function. The proposed model consists of a symmetry-respecting QNN combined with an NN, with the observable measured on the quantum state consisting only of Pauli-Z operators. The performance of the siQNN-NN and siQNN were significantly better than the performance of the models learning only on classical data for small training dataset sizes across all molecules.

From these observations, we deduce that the siQNN effectively extracts valuable information from the ground state and provides a good estimate of various target functions in this study. For very small training datasets, the additional complexity of the siQNN-NN leads to overfitting which decreases the performance relative to the siQNN. As the training dataset size increases, the siQNN,

however, struggles to describe the training data points to the given accuracy, and the additional degrees of freedom in the NN become valuable to account for the R dependence of the observable.

We note several limitations of our study. Firstly, we expect that for each target function and molecule there exist a number of training data points above which the models learning purely on the classical data reach sufficient test dataset accuracy on average and therefore the additional effort of preparing the quantum information is not reasonable anymore. This is because for all data points, the ground state needs to be provided, introducing a relevant overhead relative to models learning only on the classical data. Further, to enable our model to predict excited-state properties, training values of those properties need to be derived using another technique. Therefore, our model is relevant for molecules where the properties of interest for different geometric configurations are calculable but with significant effort, while the ground state is less computationally demanding. Given that excited-state properties are generally more complex than ground-state properties, there are several molecules and properties that meet this condition.

Secondly, the substructure of the siQNN has similarities to the structure of a quantum convolutional neural network, which is known to be simulable. This suggests the possibility that the siQNN is efficiently classically simulable. However, the envisioned use case for the procedure described in this work is a scenario where molecular ground state simulations are performed on a quantum computer. Adding a comparatively small QNN as suggested here is then a relatively small overhead to obtain excited state properties on top of ground state properties. Still, it could be an interesting further research path to construct a purely classical model inspired by our quantum-enhanced model that could extract valuable information and investigate whether it can do this even more efficiently from the ground, for example, using classical shadows [33]. Finally, this study was conducted using exact ground states. Investigating the effect of im-

perfect simulations of molecular ground states as input is an interesting research question.

In conclusion, we propose a procedure to deriving excited-state properties in an efficient way. We deem this approach valuable to analyzing molecular properties and understanding and predicting their behaviors. We view this study as a starting point for further investiga-

tions into extracting information from the ground state for excited-state properties.

ACKNOWLEDGMENTS

This work was supported by the German Federal Ministry of Economic Affairs and Climate Action through the projects AQUAS (grant no. 01MQ22003D). The authors would like to thank Jan Schnabel and David A. Kreplin for fruitful discussions. The authors disclose the use of LLM-based tools for grammar and spell-checking.

-
- [1] L. Serrano-Andrés and M. Merchán, Quantum chemistry of the excited state: 2005 overview, *Journal of Molecular Structure: THEOCHEM* **729**, 99 (2005).
- [2] I. Shahnavi, S. Ahmed, Z. Anwar, M. Sheraz, and M. Sikorski, Photostability and photostabilization of drugs and drug products, *International Journal of Photoenergy* **2016**, 1 (2016).
- [3] E. Vöhringer-Martinez and A. Toro-Labbé, Understanding the physics and chemistry of reaction mechanisms from atomic contributions: A reaction force perspective, *The Journal of Physical Chemistry A* **116**, 7419 (2012).
- [4] Y. Cao, J. Romero, and A. Aspuru-Guzik, Potential of quantum computing for drug discovery, *IBM Journal of Research and Development* **62**, 6:1 (2018).
- [5] V. von Burg, G. H. Low, T. Häner, D. S. Steiger, M. Reiher, M. Roetteler, and M. Troyer, Quantum computing enhanced computational catalysis, *Phys. Rev. Res.* **3**, 033055 (2021).
- [6] P. Knowles and N. Handy, A new determinant-based full configuration interaction method, *Chemical Physics Letters* **111**, 315 (1984).
- [7] Q. Sun, J. Yang, and G. K.-L. Chan, A general second order complete active space self-consistent-field solver for large-scale systems, *Chemical Physics Letters* **683**, 291–299 (2017).
- [8] R. Santagati, A. Aspuru-Guzik, R. Babbush, M. Degroote, L. González, E. Kyoseva, N. Moll, M. Oppel, R. M. Parrish, N. C. Rubin, M. Streif, C. S. Tautermann, H. Weiss, N. Wiebe, and C. Utschig-Utschig, Drug design on quantum computers, *Nature Physics* **20**, 549–557 (2024).
- [9] J. Tilly, H. Chen, S. Cao, D. Picozzi, K. Setia, Y. Li, E. Grant, L. Wossnig, I. Rungger, G. H. Booth, and J. Tennyson, The variational quantum eigensolver: A review of methods and best practices, *Physics Reports* **986**, 1 (2022).
- [10] R. Cleve, A. Ekert, C. Macchiavello, and M. Mosca, Quantum algorithms revisited, *Proceedings of the Royal Society of London. Series A: Mathematical, Physical and Engineering Sciences* **454**, 339–354 (1998).
- [11] A. D. Córcoles, A. Kandala, A. Javadi-Abhari, D. T. McClure, A. W. Cross, K. Temme, P. D. Nation, M. Steffen, and J. M. Gambetta, Challenges and opportunities of near-term quantum computing systems, *Proceedings of the IEEE* **108**, 1338 (2020).
- [12] S. Lee, J. Lee, H. Zhai, Y. Tong, A. Dalzell, A. Kumar, P. Helms, J. Gray, Z.-H. Cui, W. Liu, M. Kastyano, R. Babbush, J. Preskill, D. Reichman, E. Campbell, E. Valeev, L. Lin, and G. Chan, Evaluating the evidence for exponential quantum advantage in ground-state quantum chemistry, *Nature Communications* **14** (2023).
- [13] J. Ceroni, T. F. Stetina, M. Kieferova, C. O. Marrero, J. M. Arrazola, and N. Wiebe, *Generating Approximate Ground States of Molecules Using Quantum Machine Learning* (2023).
- [14] J. Robledo-Moreno, M. Motta, H. Haas, A. Javadi-Abhari, P. Jurcevic, W. Kirby, S. Martiel, K. Sharma, S. Sharma, T. Shirakawa, I. Sitdikov, R.-Y. Sun, K. J. Sung, M. Takita, M. C. Tran, S. Yunoki, and A. Mezzacapo, *Chemistry Beyond Exact Solutions on a Quantum-Centric Supercomputer* (2024).
- [15] P. B. Armentrout, Chemistry of excited electronic states, *Science* **251**, 175 (1991).
- [16] L. González, D. Escudero, and L. Serrano-Andrés, Progress and challenges in the calculation of electronic excited states, *ChemPhysChem* **13**, 28 (2012).
- [17] O. Higgott, D. Wang, and S. Brierley, Variational quantum computation of excited states, *Quantum* **3**, 156 (2019).
- [18] K. M. Nakanishi, K. Mitarai, and K. Fujii, Subspace-search variational quantum eigensolver for excited states, *Phys. Rev. Res.* **1**, 033062 (2019).
- [19] H. Kawai and Y. O. Nakagawa, Predicting excited states from ground state wavefunction by supervised quantum machine learning, *Machine Learning: Science and Technology* **1**, 045027 (2020).
- [20] Q. Yao, Q. Ji, X. Li, Y. Zhang, X. Chen, M.-G. Ju, J. Liu, and J. Wang, Machine learning accelerates precise excited-state potential energy surface calculations on a quantum computer, *The Journal of Physical Chemistry Letters* **15**, 7061 (2024).
- [21] P. Jordan and E. Wigner, ber das paulische equivalenzverbot, *Zeitschrift fr Physik* **47**, 631 (1928).
- [22] F. Vatan and C. Williams, Optimal quantum circuits for general two-qubit gates, *Phys. Rev. A* **69**, 032315 (2004).
- [23] I. Cong, S. Choi, and M. D. Lukin, Quantum convolutional neural networks, *Nature Physics* **15**, 1273 (2019).
- [24] P. Bermejo, P. Braccia, M. S. Rudolph, Z. Holmes, L. Cincio, and M. Cerezo, *Quantum Convolutional Neural Networks are (Effectively) Classically Simulable*

- (2024).
- [25] D. P. Kingma and J. Ba, [Adam: A Method for Stochastic Optimization](#) (2017).
- [26] Q. Sun, T. C. Berkelbach, N. S. Blunt, G. H. Booth, S. Guo, Z. Li, J. Liu, J. McClain, E. R. Sayfutyarova, S. Sharma, S. Wouters, and G. K.-L. Chan, [The Python-based Simulations of Chemistry Framework \(PySCF\)](#) (2017).
- [27] A. Javadi-Abhari, M. Treinish, K. Krsulich, C. J. Wood, J. Lishman, J. Gacon, S. Martiel, P. D. Nation, L. S. Bishop, A. W. Cross, B. R. Johnson, and J. M. Gambetta, [Quantum computing with Qiskit](#) (2024).
- [28] J. Ansel, E. Yang, H. He, N. Gimelshein, A. Jain, M. Voznesensky, B. Bao, P. Bell, D. Berard, E. Burovski, *et al.*, Pytorch 2: Faster machine learning through dynamic python bytecode transformation and graph compilation, in *29th ACM International Conference on Architectural Support for Programming Languages and Operating Systems, Volume 2* (ACM, 2024).
- [29] D. A. Kreplin, M. Willmann, J. Schnabel, F. Rapp, M. Hagelüken, and M. Roth, [sqlearn - a python library for quantum machine learning](#) (2023).
- [30] V. Bergholm, J. Izaac, M. Schuld, C. Gogolin, S. Ahmed, V. Ajith, M. S. Alam, G. Alonso-Linaje, B. Akash-Narayanan, A. Asadi, *et al.*, [PennyLane: Automatic differentiation of hybrid quantum-classical computations](#) (2022).
- [31] F. Pedregosa, G. Varoquaux, A. Gramfort, V. Michel, B. Thirion, O. Grisel, M. Blondel, P. Prettenhofer, R. Weiss, V. Dubourg, J. Vanderplas, A. Passos, D. Cournapeau, M. Brucher, M. Perrot, and E. Duchesnay, Scikit-learn: Machine learning in Python, *Journal of Machine Learning Research* **12**, 2825 (2011).
- [32] J. Bowles, S. Ahmed, and M. Schuld, [Better than classical? The subtle art of benchmarking quantum machine learning models](#) (2024).
- [33] H.-Y. Huang, Learning quantum states from their classical shadows, *Nature Reviews Physics* **4**, 81 (2022).

Appendix A: MSE Score Plots

Here, we show the MSE plots derived for the given models and training dataset sizes, on the different molecules and target functions, which are shown in Figure 4. From the data shown in these MSE plots, the ranking plots in Figure 7 are derived.

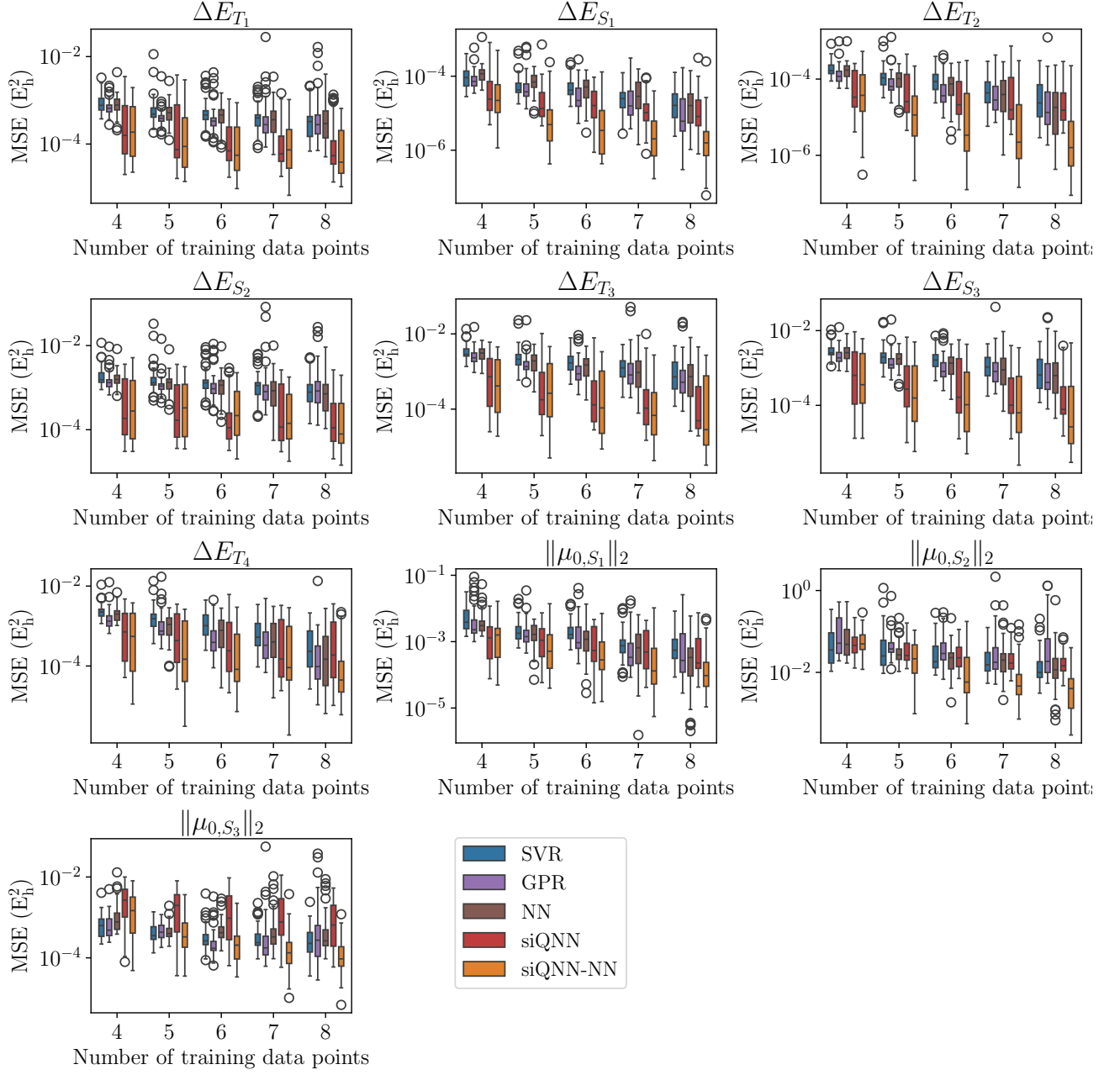


FIG. 8. Box plots of the MSE on the test datasets for 50 randomly sampled datasets \mathcal{D}_i^L for the given models and training dataset sizes L for LiH. The heading of each subplot defines the target function, that is fitted.

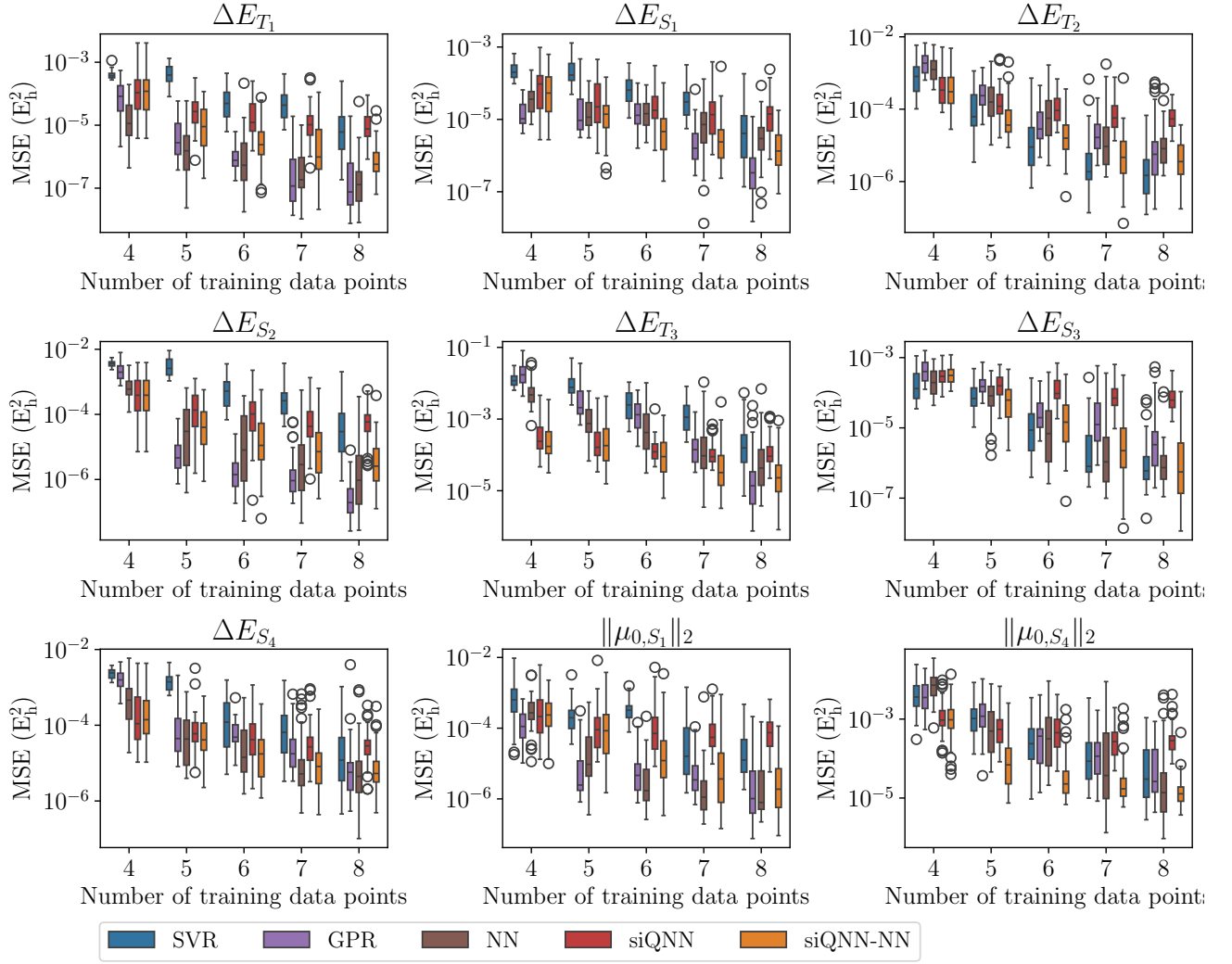


FIG. 9. Box plots of the MSE on the test datasets for 50 randomly sampled datasets \mathcal{D}_t^L for the given models and training dataset sizes L for H_2 . The heading of each subplot defines the target function, that is fitted.

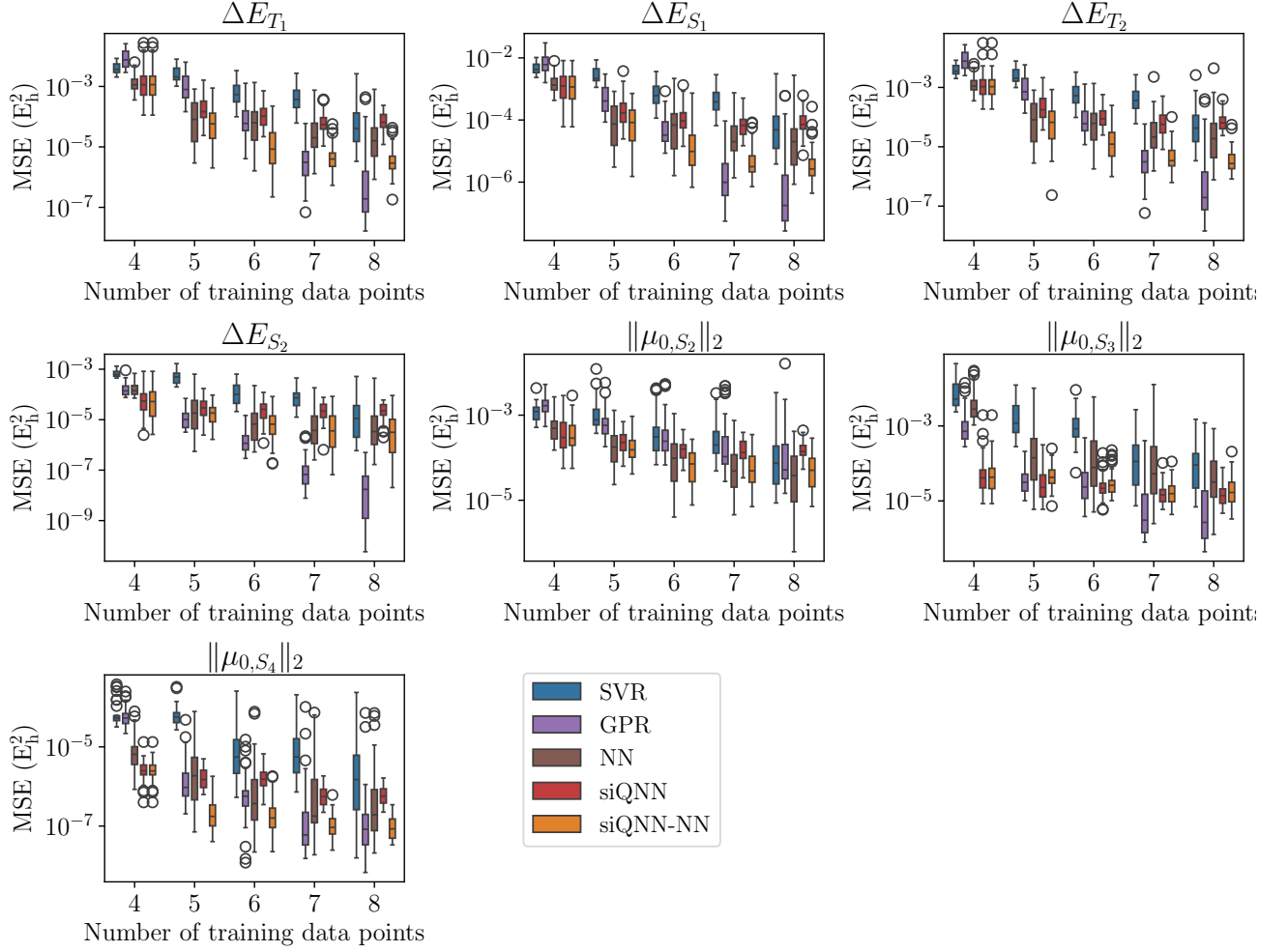


FIG. 10. Box plots of the MSE on the test datasets for 50 randomly sampled datasets \mathcal{D}_T^L for the given models and training dataset sizes L for H_4 . The heading of each subplot defines the target function, that is fitted.